Enhancement in Ti–6Al–4V sintering via nanostructured powder and spark plasma sintering

Kyle Crosby, Leon Shaw, Claude Estournès, Geoffroy Chevallier, Arne Woolsey Fliflet, M. Ashraf Imam

Enhancement in Ti–6Al–4V sintering via nanostructured powder and spark plasma sintering

K. Crosby[1], L. L. Shaw*[1,2], C. Estournes[3], G. Chevallier[3], A. W. Fliflet[4] and M. A. Imam[4]

Studies are performed to enhance low temperature sintering of Ti–6Al–4V. High energy ball milling is found to be effective in lowering the sintering temperature through the mechanisms of particle size reduction and nanograin formation. The former reduces the diffusion distance for densification, whereas the latter introduces an additional densification mechanism allowing mass transport from the interior of the particle to the neck zone. Together, these two effects can reduce the onset temperature for densification by about 300°C. Spark plasma sintering can further improve low temperature sintering when compared with radiant heat sintering and microwave sintering. The enhanced densification is discussed on the basis of the applied pressure (50 MPa) and the intrinsic joule effect that leads to increase in the local temperature at the contact point between particles.

Keywords: Titanium alloys, Ball milling, Nanomaterials, Sintering

Introduction

Currently, there is a significant need to improve fixation and performance of orthopaedic implants because of the growing elderly population. Device lifespan and bioactivity have been improved steadily since the inception of orthopaedic implants through the use of specific materials systems (e.g. bioinert metallic alloys, low modulus alloys and bioactive ceramic coatings)[1–3] and fabrication techniques (e.g. porous surface structures).[4] However, there is still a desire to further enhance the lifespan and performance of implants such that the device meets or exceeds the performance of the natural biological structure. One of the approaches to achieve this goal is to develop functionally graded implants composed of a Ti–6Al–4V (Ti–6–4) core and a hydroxyapatite (HA) rich surface. The former will provide mechanical strength, while the latter will offer a bioactive surface with no sharp interface between the core and surface. Such functionally graded implants can be fabricated via powder processing and cosintering of Ti–6–4 and HA. However, cosintering of Ti–6–4 and HA at temperatures above 1000°C results in a substantial strength reduction of Ti–6–4 due to the embrittlement of oxygen diffusion into the metal.[5] Thus, there is a critical need to study methods for sintering Ti–6–4 at temperatures <1000°C.

Sintering behaviour of Ti–6–4 has been studied by many investigators in order to obtain either porous or dense bodies.[6–14] Porous bodies or porous surface with a dense core is aimed at enhancing tissue ingrowth for Ti–6–4 orthopaedic implants,[7,10–12] whereas dense bodies can offer superior specific strength for load carrying applications.[6,8] In general, 1200°C or higher is required to obtain dense Ti–6–4 bodies. Specifically, Tasdemirci *et al.*[9] reveal that sintering at 1200°C for 2 h only results in Ti–6–4 bodies that still contain 38 vol.-% porosity. The same sintering result is reported by Guden *et al.*[14] Shibo and his co-workers[6] show that depending on the binder used in the powder injection moulding process, powder injection moulded Ti–6–4 bodies can reach a relative density of either 97 or 94% of the theoretical density after sintering at 1230°C for 3 h. They further demonstrate that uniaxial pressing of the same Ti–6–4 powder followed by sintering at 1230°C for 3 h can only lead to a relative density of 95%, similar to the powder injection moulded bodies. Bautista *et al.*[13] have sintered Ti–6–4 bodies at different conditions and have shown that Ti–6–4 bodies still contain about 0·5% porosity after sintering at 1260°C for 4 h. When the sintering temperature is reduced to 1230 and 1200°C, the porosity level is increased to 1 and 1·3% respectively.[13] All of these studies reveal one common phenomenon, that is pressureless sintering of Ti–6–4 requires sintering temperatures at 1200°C or higher in order to reduce porosity in the sintered bodies.

[1]Department of Chemical, Materials & Biomolecular Engineering, University of Connecticut, Storrs, CT 06269, USA
[2]Department of Mechanical, Materials, and Aerospace Engineering, Illinois Institute of Technology, Chicago, IL 60616, USA
[3]CNRS, Univsersité de Toulouse, Institut Carnot CIRIMAT, 118 route de Narbonne, Toulouse 31062, France
[4]Materials Science and Component Technology Directorate, Naval Research Laboratory, Washington, DC 20375, USA

*Corresponding author, email lshaw2@iit.edu

DOI 10.1179/1743290113Y.0000000082

In order to obtain fully dense Ti–6–4 bodies, pressure is often applied during sintering. For example, Shibo *et al.*[6] demonstrate that Ti–6–4 bodies with 99·3% density can be obtained by pressureless sintering at 1230°C for 3 h, followed by hot isostatic pressing at 1230°C again. Kim and Yang[8] also reveal that by applying a pressure of 60 MPa during hot pressing (HP), Ti–6–4 bodies with density higher than 99% can be obtained after HP at 950°C for 2 h. However, HP at 850°C for 2 h is not sufficient to obtain Ti–6–4 bodies with density higher than 99%.[8]

Clearly, there are challenges in attaining dense Ti–6–4 bodies at sintering temperature below 1000°C. In this study, we focus on the investigation of processing of nanostructured Ti–6–4 powder along with different sintering methods in order to achieve sintering of fully dense Ti–6–4 bodies at 1000°C or lower. This study will pave the way to achieve co-sintering of Ti–6–4 and HA at temperatures compatible with the stability domain of HA and prevention of Ti–6–4 embrittlement (i.e. $<$1000°C) in the near future. The detail of attaining nanostructured Ti–6–4 and sintering at temperatures below 1000°C is described below.

Materials and methods

The commercial Ti–6–4 powder was purchased from Advanced Specialty Metals (Nashua, NH, USA). The as received powder is composed of highly uniform spherical particles in the range of 45–250 μm in diameter. High energy ball milling under inert argon atmosphere was performed using a SPEX mill with a ball/powder weight ratio of 10 : 1. To prevent excessive cold welding during ball milling, stearic acid was added to the powder as a process control agent (PCA). The concentration of stearic acid ranging from 1 to 5 wt-% was investigated in order to identify the proper concentration of PCA for achieving the smallest crystallite size of Ti–6–4 along with the minimum particle size. To avoid substantial heating during ball milling that can also lead to excessive cold welding, long duration ball milling was conducted using short 1 h milling increments followed by 15 min of cooling at room temperature. On the basis of these investigations, Ti–6–4 powder with the smallest crystallite size was selected for sintering studies.

Sintering investigation was performed using three different methods, that is traditional radiant heat sintering (RHS), spark plasma sintering (SPS) and microwave sintering (MWS). Radiant heat sintering was conducted using an alumina tube with steel end caps which allow for atmospheric control. Green body pellets were prepared with a stainless steel die by using 300 MPa uniaxial pressure. To prevent oxidation during sintering, pellets were wrapped in tantalum foil and sealed in quartz tubing under a vacuum of less than 10 mT before their insertion into the alumina tube, which was evacuated and purged with argon before the onset of heating. Spark plasma sintering was performed at the Plateforme Nationale CNRS de Frittage-Flash (PNF^2, Toulouse) using a Dr Sinter 2080 (SPS Syntex Inc., Japan). The desired amount of Ti–6–4 powder was loaded into a graphite die of 8 mm in diameter. For easy removal of the sintered pellet, a sheet of graphitic paper was placed between the punch and the powder as well as between the die and the powder to prevent sticking due to any possible reaction between the powder and graphite die/punch. A uniaxial pressure of 50 MPa was applied throughout the process. Sintering was conducted under vacuum, and the heating rate was 100°C min^{-1}. Changes in temperature, average intensity and voltage of the pulsed current and sintering displacement were recorded *in situ* by a computer during the entire sintering process. The thermocouple for monitoring the temperature was placed in a little hole 3 mm in depth at the surface of the graphite die. Thus, the measured value corresponds to the temperature of the inner surface of the die near the sample. However, because of the high thermal conductivity of graphite and Ti–6–4, the sample temperature would be close to the thermocouple reading. The sintering displacement curves were used to identify the onset and completion temperatures of densification during continuous heating. The green pellets 0·5 inch in diameter for MWS were formed using 670 MPa uniaxial pressure, followed by 690 MPa isostatic pressing at room temperature. The green pellets were then placed inside an insulated chamber. No susceptor material was used due to the particle–pore dipole interaction that suffices to generate heat within the sample. The microwaves were generated in a 2·45 GHz Cober Electronics Model S6F Industrial Microwave Generator and transported to the heating chamber via S band waveguide.

Scanning electron microscopy (SEM) was used to examine the average powder particle size as a function of milling duration. Samples for particle size measurements were prepared by dry dropping of the powder particles onto copper tape that was mounted on an SEM sample stub. Quantification via SEM involved direct measurement of the powder particles using a calibration based on the scale bar specific to the magnification displayed on each image. Approximately 15 particles were measured from each of five images of the same SPEX milling powder condition. As such, the average particle size calculation took into account the distribution of particle sizes over $>$50 particles. Scanning electron microscopy analysis was also conducted to examine the microstructure and porosity of sintered samples. On the basis of the porosity at the polished cross-section, the densities of sintered samples were determined. For microstructural characterisation of the as received and ball milled powders, powders were mounted in conductive copper mounting compound, ground to 1200 grit SiC roughness and then polished to a mirror finish using 0·05 μm colloidal silica. After a uniform surface was attained, the sample was swabbed with Kroll's etchant until the microstructure had reasonable contrast under the optical microscope.

X-ray diffraction (XRD) (Bruker D2 Phaser, Madison, WI, USA) studies were conducted for each SPEX milled sample to determine phase purity and monitor any compounds that may be forming during the milling process using Cu K_α radiation, 30 V, 10 mA, 0·02°/step and 0·26 s/step scan rate. In addition to monitoring phase formation, XRD was also used to estimate the crystallite size via peak broadening through the use of the Scherrer formula[15]

$$\beta_g = k\lambda / D\cos\theta \quad (1)$$

where β_g is the full width half maximum peak breadth, k is the shape factor ($\sim$1·0), λ is the X-ray wavelength (Cu $K_{\alpha 1}$=1·541 nm), D is the crystallite size and θ is the Bragg angle. In this study, the reflections used for the crystallite

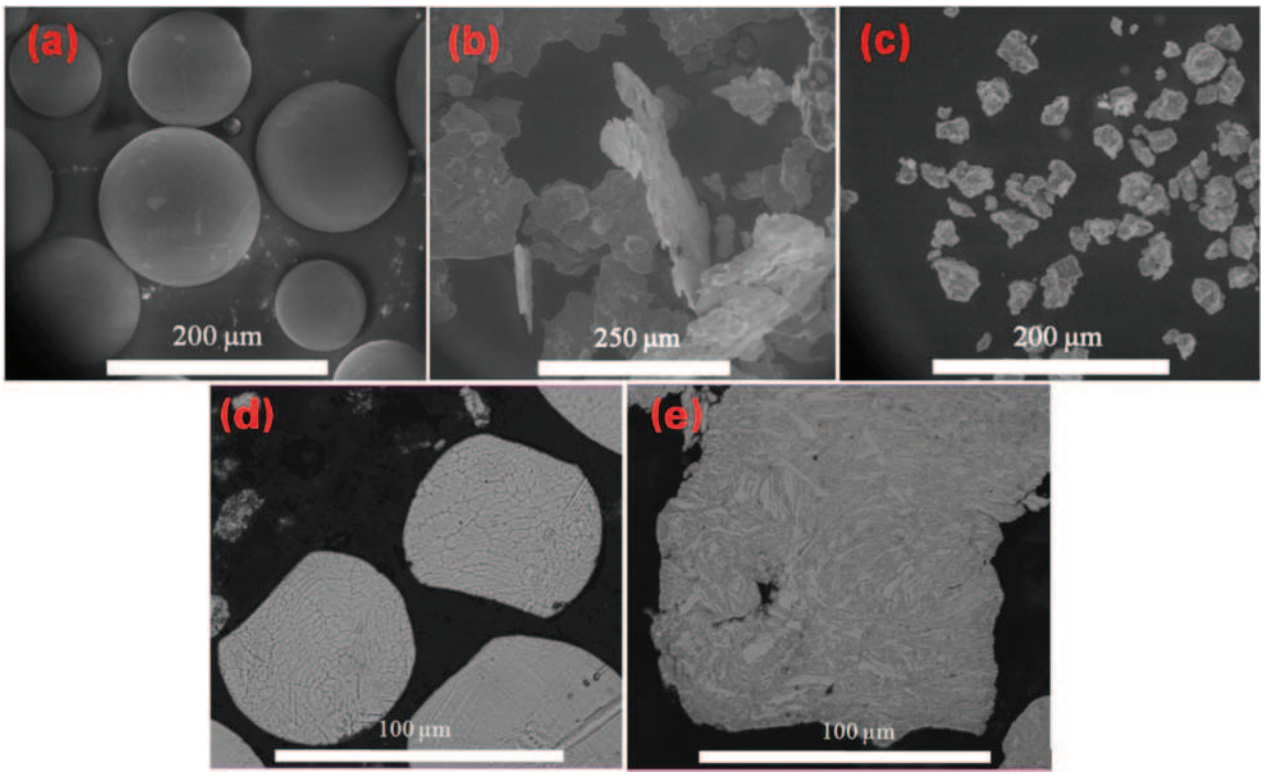

a as received; *b* ball milled for 1 h; *c* ball milled for 4 h; *d* etched cross-section of as received; *e* etched cross-section of ball milled for 4 h

1 Images of Ti–6–4 powder

size estimation were at low 2θ angles (to be provided in the section on 'Results and discussion'). Since the reflections used for the crystallite size estimation were at low 2θ angles and the instrumental broadening of our instrument was small, the broadening was therefore mainly attributed to ultrafine crystallites.[16]

To verify the crystallite size estimation via the XRD line broadening, transmission electron microscopy (TEM) analysis of ball milled samples was performed. The TEM samples were prepared by ultrasonicating the ball milled powder in ethanol for 15 min to suspend the fine particles. A pipette was used to dispense a few suspension drops to an ultrathin carbon film (Ted Pella TEM product). The drops were allowed to dry in air. The operating condition of the TEM (FEI Tecnai Spirit Twin TEM) was 120 kV in either bright or dark field imaging modes.

Results and discussion

Particle size reduction and nanostructure formation through high energy ball milling

Figure 1 shows the evolution of the shape and microstructure of Ti–6–4 particles induced by ball milling. One hour ball milling has changed the initial spherical particles with an average diameter of 120 μm (Fig. 1*a*) to large flakes with a thickness of ~25 and 150 μm in diameter (Fig. 1*b*). Further ball milling up to 4 h leads to equiaxed particles with an average diameter of ~25 μm (Fig. 1*c*). However, prolonged milling beyond the 4 h duration yields little change in the particle morphology and the average particle diameter, indicating that a balance between cold welding and fracture has been reached at ~4 h milling for the material with 4 wt-% stearic acid. Such morphology evolution is consistent with the behaviour of ductile phases subjected to high energy ball milling observed previously.[17–19] That is the formation of plate-like morphology at the early stage of milling due to severe plastic deformation via 'mini forging', which is followed by repeated particle fracture once the ductility of particles is exhausted. Finally, the extensive particle fracture is balanced by cold welding, leading to the final particle sizes that are insensitive to the prolonged milling time.

In addition to the particle morphology evolution, the microstructure of particles has been altered as well. The as received powder particles show a dendritic microstructure with a dendrite arm thickness of ~4 μm, indicative of slow cooling from a melt (Fig. 1*d*). When ball milling is performed, the dendritic microstructure is replaced by an elongated lamellar microstructure with a thickness of ~1 μm (Fig. 1*e*). Such microstructure evolution is due to continual plastic deformation and cold welding during the ball milling process. Although nanograin formation cannot be detected using SEM, the XRD and TEM analyses below indicate that the microstructure change at the nanometre level also takes place during ball milling.

Figure 2 shows the XRD spectra of Ti–6–4 as a function of the milling time. It can be seen that the crystallite size decreases continuously with increased milling duration, as indicated by the continuous peak broadening when the milling time increases. The coherent XRD domain size (termed as the crystallite size hereafter) of Ti–6–4 has been estimated using the Scherrer formula.[15] The two major reflections, (101) and (002), of Ti–6–4 are utilised for such estimation. The values obtained are listed in Table 1. As shown, the peak

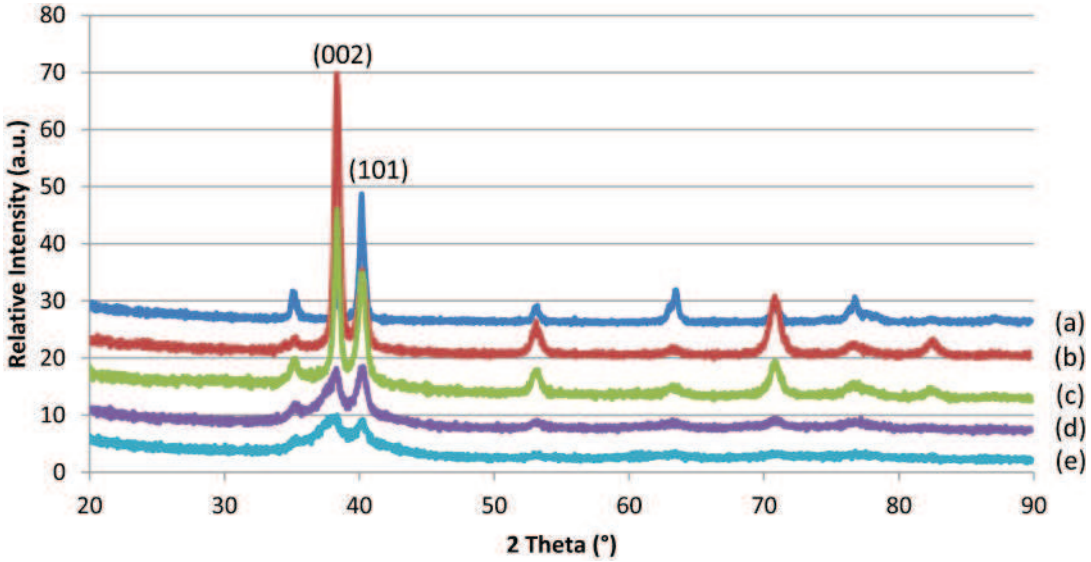

a as received; *b* ball milled for 1 h; *c* ball milled for 2 h; *d* ball milled for 3 h; *e* ball milled for 4 h (all are with 4 wt-% stearic acid)

2 X-ray diffraction spectra of Ti–6–4 samples

broadening analysis of both reflections reveals that the crystallite sizes of Ti–6–4 powder decrease continually as the milling time increases. With 4 h milling, the crystallite sizes have been reduced to 35 or 15 nm, depending on which reflection is considered. In contrast, the crystallite size for the as received particles is beyond the valid range of the Scherrer formula (i.e. >100 nm). The estimation of crystallite sizes was corroborated using the TEM analysis. As shown in Fig. 3, the Ti–6–4 powder after 4 h of ball milling with the presence of 4 wt-% stearic acid exhibits many grains with sizes in the order of 10–20 nm. These observations are consistent with the expectation that sufficient high energy ball milling will result in the formation of nanograins within ductile particles.[18–23] The formation of nanograins in ductile phases has been shown to proceed by substantial/increases in dislocation density, followed by the disintegration of the crystal into subgrains separated by low angle grain boundaries, and a gradual increase in subgrain boundary misorientation, which eventually leads to the full evolution of nanograins.[20,21]

The effect of the PCA concentration on the particle size and crystallite size as a function of milling time is shown in Fig. 4. The data for the 1 wt-%PCA addition are not included in this figure because of severe cold welding of the powder to the walls of the milling vial. Figure 4 shows clearly that the average particle size decreases with increasing the PCA concentration. This is consistent with the expectation because the function of PCA is to prevent cold welding.[19] Therefore, the more PCA, the more effective in preventing cold welding and thus the smaller particle size. It is interesting to note that the average crystallite size also decreases with increasing the PCA concentration until a critical concentration (~4 wt-% for 4 h milling) is reached. We propose that this phenomenon arises because of two competing processes. First, the initial increase in the PCA concentration results in smaller particle sizes, as shown in Fig. 4*a*. The decreased particle size leads to more effective plastic deformation of the particle and thus results in higher dislocation densities in the particle. The latter in turn translates to faster grain size reduction because the formation of nanograins requires the accumulation of plastic strain to a critical value.[24] Second, after the PCA concentration reaches a critical value (~4 wt-% for 4 h milling), further increase in PCA does not lead to reduction in the grain size; instead, it may result in a slight increase in the grain size as shown in Fig. 4*b*. This is due to the lubricating effect of PCA and has been observed in ball milling of Al alloys previously.[19]

Table 1 X-ray diffraction analysis of crystallite sizes as function of milling duration

Milling duration/h	(101) crystallite size/nm	(002) crystallite size/nm
0 (as received)	>100	>100
1	51	77
2	53	76
3	44	21
4	35	15

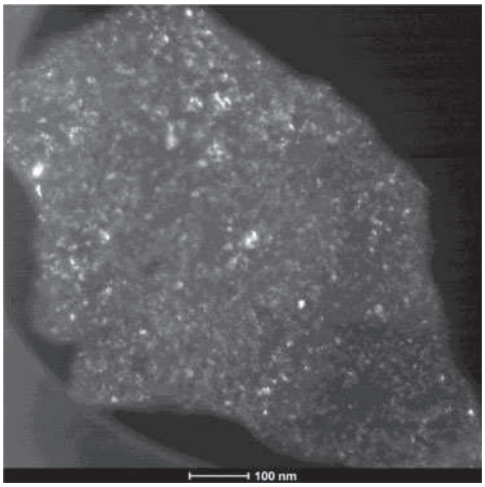

3 Dark field TEM image of Ti–6–4 powder ball milled for 4 h with presence of 4 wt-% stearic acid

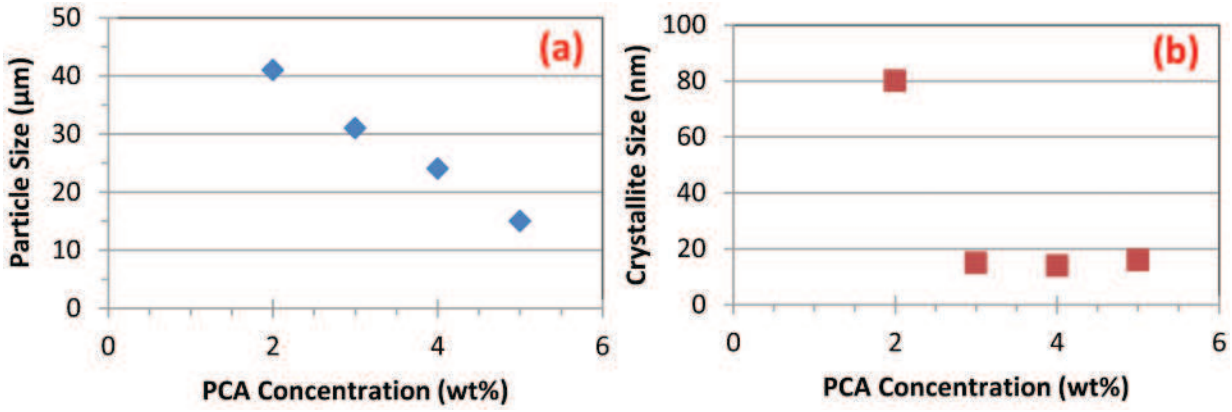

4 *a* average particle size (via SEM image analysis) and *b* average crystallite size [via XRD analysis of (002) reflection] of Ti–6Al–4V powder ball milled for 4 h as function of PCA concentration

Based on the reduced particle and crystallite sizes, we expect that sintering kinetics will be improved. Furthermore, we have chosen the Ti–6–4 powder ball milled for 4 h with the addition of 4 wt-% stearic acid for detailed sintering studies because this powder exhibits the lowest crystallite size along with the second smallest particle size. The sintering behaviour of this powder is described below.

Sintering enhancement via nanostructured powder

Figure 5 presents the microstructure of Ti–6–4 samples sintered under various conditions. The as received powder only results in a porous body after sintering at 1250°C for 2 h via RHS (Fig. 5*a*). The fraction of the solid area determined using the ImageJ image analysis software (National Institutes of Health, USA) is found to be ~90%. However, 4 h ball milling before sintering has reduced porosity drastically and increased the sintered density to 97% of the theoretical (Fig. 5*b*). With SPS, the sintered density can reach >99% even with the use of the as received powder and continuous heating up to 860°C only (Fig. 5*c*). In contrast, MWS exhibits similar sintered densities as RHS, showing a density of 98% at the central region (Fig. 5*d*) and a density of 81% at the edge (not shown here) after sintering at 1250°C for 30 min. The densities of all other samples sintered under different conditions are summarised in Table 2. It is interesting to note that the sintered density for the 1 h ball milled powder sintered using RHS is only 75% of the theoretical, even lower than the density sintered from the as received powder.

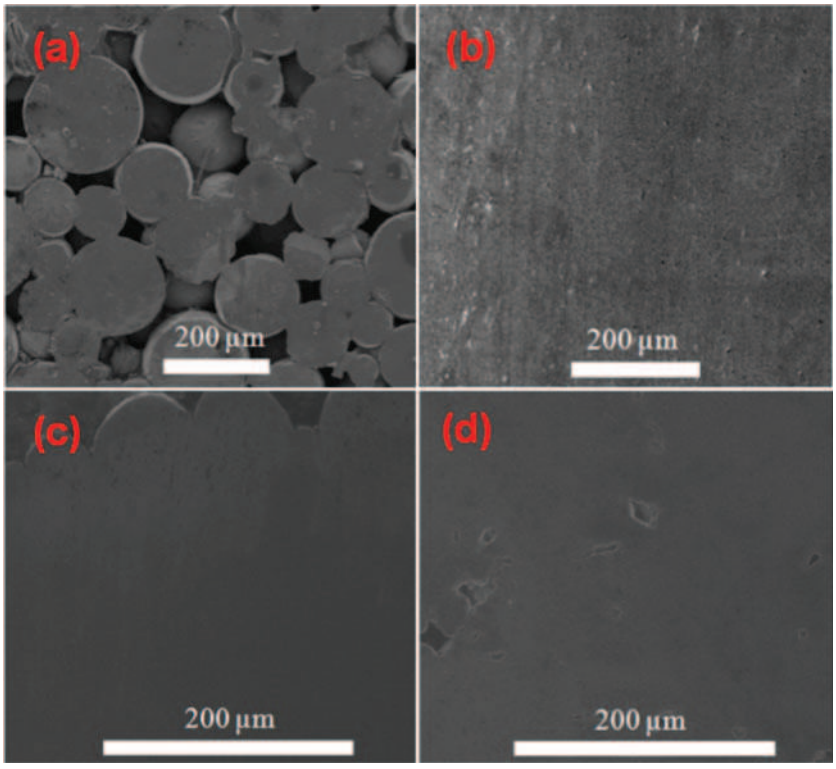

a as received powder sintered at 1250°C for 2 h via RHS; *b* 4 h ball milled powder sintered at 1250°C for 2 h via RHS; *c* as received powder sintered via SPS with completion of shrinkage at 860°C during continuous heating; *d* core region of 4 h ball milled powder sintered at 1250°C for 30 min via MWS

5 Polished surfaces of sintered pellets

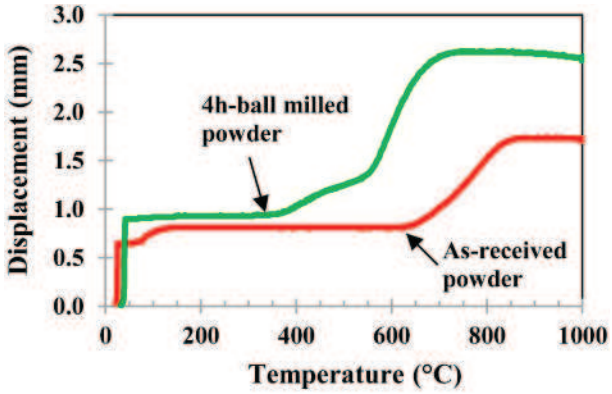

6 Punch displacement curves during SPS with heating rate of 100°C min^{-1}; arrows point to onset temperature for shrinkage during continuous heating for powder compacts indicated

This is due to the formation of elongated plate-like particles after 1 h ball milling (Fig. 1*b*). These elongated plate-like particles do not pack well during uniaxial pressing, which is performed at a pressure below the yield strength of Ti–6–4. Therefore, the large pore volume and folding/unfolding of the plate-like particles prevent the achievement of high green density and thus lead to the low sintered density.

Note that the low density of the sintered bodies derived from the as received powder is in good accordance with other studies. Specifically, using Ti–6–4 particles with a mean diameter of 170 μm and sintering at 1200°C for 2 h, Tasdemirci *et al.*[9] have obtained a sintered body of only 62% dense. In contrast, densification behaviour improves noticeably when the powder particle size decreases. For example, using Ti–6–4 powder with particle sizes ranging from 25 to 45 μm and pressing followed by sintering at 1230°C for 3 h, Shibo *et al.*[6] have achieved sintered bodies of 94·6% dense. Although a precise comparison cannot be made between the present study and previous ones because of different sources of powders and different packing densities before sintering, the trend of the present study showing improved densification with decreasing particle sizes is consistent with previous investigations.[6,9,14]

For the present study, the drastically improved densification behaviour of 4 h ball milled Ti–6–4 samples versus the as received powder can be attributed to two factors. First, the particle size has been reduced from ~120 to 25 μm. This particle size reduction will translate into a shorter diffusion distance from the interparticle boundary area to the neck zone of the particles, and thus enhance the densification rate, as predicted by Herring's scaling law.[25] Second, the crystallites of the ball milled particles have been reduced to ~35 nm or less, indicating the formation of nanograins within micrometre sized particles. As pointed out before, many metals exhibit the same behaviour as Ti–6–4 in this study, that is they become nanostructured particles after sufficient high energy ball milling.[18–23] The presence of the nanograins will greatly increase the grain boundary area within each particle, and thus the diffusion flux of the atoms from the interior of the particle to the neck zone of the particles. The presence of this nanostructure effect can be confirmed by analysing the onset temperature for densification of the as received and 4 h ball milled samples during SPS. As shown in Fig. 6, the onset temperature for densification has been reduced from 893 K (620°C) for the as received powder to 613 K (340°C) for the 4 h ball milled sample. It is well known that at the initial stage of sintering, the shrinkage is related to neck growth through equation (2)[26]

$$\frac{\Delta L}{L_0} = \left(\frac{x}{D}\right)^2 \tag{2}$$

where the shrinkage $\Delta L/L_0$ is the length change divided by the initial length, x is the neck diameter and D is the particle diameter. The neck size ratio x/D is in turn correlated to the particle diameter, sintering time t, sintering temperature T and the primary mechanism of mass transport for densification.[26] Assuming that the primary mechanism for densification is the mass transport from the interparticle boundary area to the neck zone through interparticle boundary diffusion, one will have the following relationship[26]

$$\left(\frac{x}{D}\right)^6 = B_0 \exp\left(-\frac{Q_{gb}}{RT}\right)\frac{t}{D^4} \tag{3}$$

where Q_{gb} is the activation energy for interparticle boundary diffusion, which is close to that for grain boundary diffusion; B_0 is a constant related to the interparticle boundary width, surface energy and atomic volume; and t and T have been defined above.

Since Ti–6–4 at the annealed condition is composed of ~90% of the α phase and 10% of the β phase,[27] one can use the activation energy for grain boundary self diffusion in α-Ti (Q_{gb}=187 kJ mol^{-1})[28] to estimate the neck size ratio as a function of the sintering time, sintering temperature and particle diameter. Substituting the onset temperatures of 893 K for the as received powder (D=120 μm) and 613 K for the 4 h ball milled sample (D=25 μm) with the same sintering time (e.g. 1 s at 893 K for the as received powder and at 613 K for the 4 h ball milled powder) into equation (3), one can find that the

Table 2 Density values of Ti–6–4 bodies sintered via various methods and conditions*

Sample condition	Density/%$_{theor}$
As received powder, sintered at 1250°C, 2 h, RHS	90
1 h ball milled powder, sintered at 1250°C, 2 h, RHS	75
4 h ball milled powder, sintered at 1250°C, 2 h, RHS	97
As received powder, shrinkage completion at 860°C, SPS	99+
4 h ball milled powder, shrinkage completion at 740°C, SPS	99+
4 h ball milled powder, heated to 600°C and hold for 5 min, SPS	96
4 h ball milled powder, sintered at 1250°C, 0·5 h, MWS	98 centre, 81 edge
4 h ball milled powder, sintered at 900°C, 1 h, MWS	95 centre, 80 edge

*All samples are made from the 4 h ball milled Ti–6–4 with 4 wt-% stearic acid unless indicated otherwise.

ratio of (x/D) for the as received powder to (x/D) for the 4 h ball milled powder is 185. In other words, if the shrinkage of the 4 h ball milled powder at the initial stage of sintering depends only on the mass transport from the interparticle boundary area to the neck zone, the neck size ratio of the 4 h ball milled sample would be about two orders of magnitude smaller than that of the as received powder sample. Since the neck size ratio of the 4 h ball milled sample at 613 K is similar to that of the as received powder sample at 893 K (as evidenced by the similar shrinkage at 893 and 613 K for the as received and 4 h ball milled powders respectively, shown in Fig. 6), one can conclude that neck growth for the 4 h ball milled sample does not rely only on the mass transport from the interparticle boundary area to the neck zone. The mass transport from the particle interior to the neck zone, due to substantial nanograin boundaries inside each particle, must also contribute to the neck growth and densification of the 4 h ball milled sample. Therefore, high energy ball milling has resulted in two beneficial effects on sintering of Ti–6–4. These are reduced particle sizes and the formation of nanostructure within each particle.

It should be pointed out that high energy ball milling can also activate the surface of particles and increase their reactivity.[29–33] Thus, one may argue that high energy ball milling also leads to enhanced surface diffusion due to the activated surface. However, it is well known that mass transport through surface diffusion does not result in densification of a powder compact.[34] Thus, the contribution of enhanced surface diffusion to densification, if any, should be negligible. Therefore, the enhanced densification observed for the 4 h ball milled sample should be attributed to particle size reduction and nanograin formation, as discussed above.

Densification enhancement through SPS

The present study also reveals that the densification behaviour of Ti–6–4 can be improved immensely via SPS. As shown in Table 2, the as received powder only leads to in a porous body after sintering at 1250°C for 2 h via RHS. In sharp contrast, a dense body can be formed via SPS during continuous heating up to 860°C with a heating rate of 100°C min^{-1}. For the 4 h ball milled powder, the enhancement is equally impressive. A sintered body of 97% dense can be obtained via RHS at 1250°C for 2 h. However, a sintered body of >99% dense is obtained by continuous heating up to 740°C only for SPS. This represents a reduction of more than 500°C in the sintering temperature when RHS is replaced by SPS. Furthermore, it is noted that by adding a short holding time at a preselected temperature the densification temperature of SPS can be further reduced. For example, continuous heating up to 600°C with a holding time of 5 min via SPS has resulted in a sintered body of 96% dense, indicating that with a finite holding time the completion temperature for densification via SPS can be reduced by as much as 650°C from 1250°C for RHS.

The enhanced densification properties exhibited by SPS could be ascribed to two mechanisms. First, the uniaxial pressure of 50 MPa can force particle rearrangement and the breakdown of agglomerates as well as inducing plastic deformation at high temperatures. The latter can be supported by the fact that Ti–6–4 can plastically deform under 50 MPa with a strain rate of 10^{-3} s^{-1} at 775°C.[35] In addition, it should be noted that the enhancement in densification is not due to the uniaxial pressure of 50 MPa only. The intrinsic joule effect derived from the pulsed current during SPS also plays an important role. A previous study[8] on the effect of uniaxial pressure using experiments and finite element modelling has revealed that applying 60 MPa with a holding time 10 min at 750°C only results in a Ti–6–4 body with <80% dense. In the present study, a fully dense body is obtained by continuous heating up to 740°C with a heating rate of 100°C min^{-1} for SPS. Clearly, SPS has led to a far better result than the case of applying 60 MPa at 750°C for 10 min. Thus, the intrinsic joule effect derived from the pulsed current during SPS must also play a role in enhancing densification. Since Ti–6–4 is a conducting material, a fraction of the pulsed current can flow through the powder compact resulting in heating by intrinsic joule effect. This effect is particularly important at the contact point between particles where the current density is concentrated, resulting in an increase in the local temperature and the enhanced diffusion.[36–38] In addition, the applied current can enhance sintering via non-thermal effects, such as enhanced defect mobility, point defect generation and electromigration.[39]

It is worth pointing out that the improved densification behaviour of SPS over HP has also been reported for commercially pure Ti powder.[40] It has been shown that SPS can result in dense Ti bodies at 730°C, while the same Ti powder would require 950°C to become dense bodies by using HP.[40] Another study[41] shows that commercial Ti powder (<45 μm in size) can reach 99% density at 800°C using SPS, again demonstrating that SPS can lead to low temperature densification of Ti powder, while this is not achievable through HP and RHS.

Microwave sintering behaviour

Unlike SPS, MWS, which relies on microwave energy to stimulate solid state diffusion for densification, exhibits similar sintering properties for Ti–6–4 as RHS. In MWS, the porosity of the green body allows penetration of the microwave fields into the metallic compact. These fields induce eddy currents on particle surfaces, resulting into heat generation.[42] Thus, fully dense metallic bodies like Ti–6–4 are relatively difficult to attain via MWS. Nevertheless, slightly improved densification behaviour over RHS has been observed, as evidenced by 98% density at the centre of the as received powder sample sintered at 1250°C for 0·5 h (Table 2). However, microwave sintered samples show a gradient in density from the centre of the pellet to the edge. This phenomenon stems from the microwave interaction with the sample and cooler chamber surfaces causing heat emanating from the centre of the sample to flow outward. The gradient in heating within the pellet causes the sintered body to show a large amount of porosity near the edges, with nearly full density at the core where the thermally driven diffusion process is more prominent. This is different from RHS that involves heating from the outside of the pellet. In spite of different heating mechanisms, RHS and MWS exhibit similar sintering effectiveness for Ti–6–4, as revealed in this study.

Conclusions

In summary, the present study has revealed that high energy ball milling of Ti–6–4 can greatly enhance sintering properties of Ti–6–4 powder via two mechanisms. One is the reduction of particle sizes and the other

is the formation of nanostructure within each particle. The former reduces the diffusion distance for densification, whereas the latter introduces an additional densification mechanism allowing mass transport from the interior of the particle to the neck zone. Together, these two effects can reduce the onset temperature for densification by $\sim$300°C. SPS exhibits substantial advantages over RHS and MWS, achieving nearly full theoretical density in less than 5 min of sintering at 600°C. This is well below the critical temperature of 1000°C that must be avoided for co-sintering of Ti–Al–V and HA composites. Thus, SPS is a viable option for the functionally graded orthopaedic implants. The reduction in the densification temperature achieved via SPS over RHS by as much as 650°C is attributed to particle sliding and plastic deformation at high temperatures due to the presence of the applied pressure (50 MPa) and the intrinsic joule effect that results in an increase in the local temperature at the contact point between particles.

Acknowledgement

This work was supported by the US National Science Foundation through contract no. CBET-0930365.

References

1. M. Niinomi: 'Recent metallic materials for biomedical applications', *Metall. Mater. Trans. A*, 2002, **33A**, 477–486.
2. M. Niinomi: 'Mechanical biocompatibilities of titanium alloys for biomedical applications', *J. Mech. Behav. Biomed. Mater.*, 2008, **1**, 30–42.
3. X. Hu, H. Shen, Y. Cheng, X. Xiong, S. Wang, J. Fang and S. Wei: 'One-step modification of nano-hydroxyapatite coating on titanium surface by hydrothermal method', *Surf. Coat. Technol.*, 2010, **205**, 2000–2006.
4. M. M. Dewidar and J. K. Kim: 'Properties of solid core and porous surface Ti–6Al–4V implants manufactured by powder metallurgy', *J. Alloys Compd*, 2008, **454**, 442–446.
5. M. Wei, A. J. Ruys, M. V. Swain, B. K. Milthorpe and C. C. Sorrell: 'Hydroxyapatite-coated metals: interfacial reactions during sintering', *J. Mater. Sci.: Mater. Med.*, 2005, **16**, 101–106.
6. S. B. Guo, X. H. Qu, X. B. He, T. Zhou and B. H. Duan: 'Powder injection molding of Ti–6Al–4V alloy', *J. Mater. Process. Technol.*, 2006, **173**, 310–314.
7. Y. J. Jo, C. M. Lee, H. S. Jang, N. S. Lee, J.-H. Suk and W. H. Lee: 'Mechanical properties of fully porous and porous-surfaced Ti–6Al–4V implants fabricated by electro-discharge-sintering', *J. Mater. Process. Technol.*, 2007, **194**, 121–125.
8. K. T. Kim and H. C. Yang: 'Densification behavior of titanium alloy powder during hot pressing', *Mater. Sci. Eng. A*, 2001, **A313**, 46–52.
9. A. Tasdemirci, A. Hızal, M. Altındis, I. W. Hall and M. Guden: 'The effect of strain rate on the compressive deformation behavior of a sintered Ti6Al4V powder compact', *Mater. Sci. Eng. A*, 2008, **A474**, 335–341.
10. W. H. Lee and C. Y. Hyun: 'Fabrication of fully porous and porous-surfaced Ti–6Al–4V implants by electro-discharge-sintering of spherical Ti–6Al–4V powders in an one-step process', *J. Mater. Process. Technol.*, 2007, **189**, 219–223.
11. M. M. Dewidar and J. K. Lim: 'Properties of solid core and porous surface Ti–6Al–4V implants manufactured by powder metallurgy', *J. Alloys Compd*, 2008, **454**, 442–446.
12. R. Nicula, F. Luthen, M. Stir, B. Nebe and E. Burkel: 'Spark plasma sintering synthesis of porous nanocrystalline titanium alloys for biomedical applications', *Biomol. Eng.*, 2007, **24**, 564–567.
13. A. Bautista, C. Moral, G. Blanco and F. Velasco: 'Influence of sintering on the corrosion behavior of a Ti–6Al–4V alloy', *Mater. Corros.*, 2005, **56**, 98–103.
14. M. Guden, T, E. Celik, E. Akar and S. Cetiner: 'Compression testing of a sintered Ti6Al4V powder compact for biomedical applications', *Mater. Charact.*, 2005, **54**, 399– 408.
15. H. P. Klug and L. E. Alexander: 'X-ray diffraction procedures for polycrystalline and amorphous materials'; 1954, London, John Wiley & Sons, Inc.
16. L. Shaw, J. Villegas, H. Luo and D. Miracle: 'Thermal stability of nanostructured $Al_{93}Fe_3Ti_2Cr_2$ alloys prepared via mechanical alloying', *Acta Mater.*, 2003, **51**, 2647–2663.
17. B. J. M. Aikin and T. H. Courtney: 'The Kinetics of composite particle formation during mechanical alloying', *Metall. Trans. A*, 1993, **24A**, 647–657.
18. M. Zawrah and L. Shaw: 'Microstructure and hardness of nanostructured Al–Fe–Cr–Ti alloys through mechanical alloying', *Mater. Sci. Eng. A*, 2003, **A355**, 37–49.
19. L. Shaw, M. Zawrah, J. Villegas, H. Luo and D. Miracle: 'Effects of process control agents on mechanical alloying of nanostructured aluminum alloys', *Metall. Mater. Trans. A*, 2003, **34A**, 159–170.
20. H. J. Fecht, E. Hellstern, Z. Fu and W. L. Johnson: 'Nanocrystalline metals prepared by high-energy ball milling', *Metall. Trans. A*, 1990, **21A**, 2333–2337.
21. A. Belyakov, T. Sakai, H. Miura and K. Tsuzaki: 'Grain refinement in copper under large strain deformation', *Philos. Mag. A*, 2001, **81A**, 2629–2643.
22. C. C. Koch: 'The synthesis and structure of nanocrystalline materials produced by mechanical attrition: a review', *Nanostruct. Mater.*, 1993, **2**, 109–129.
23. C. Suryanarayana: 'Mechanical alloying and milling', *Prog. Mater. Sci.*, 2001, **46**, 1–184.
24. M. Umemoto, K. Todaka and K. Tsuchiya: 'Formation of nanocrystalline structure in carbon steels by ball drop and particle impact techniques', *Mater. Sci. Eng. A*, 2004, **A375**–**A377**, 899–904.
25. C. Herring: 'Effect of change of scale on sintering phenomena', *J. Appl. Phys.*, 1950, **21**, 301–303.
26. R. M. German: 'Powder metallurgy science', 2nd edn; 1994, Princeton, NJ, Metal Powder Industries Federation.
27. C. R. Brooks: 'Heat treatment, structure and properties of nonferrous alloys'; 1990, Materials, Park, OH, American Society for Metals.
28. C. Herzig, T. Wilger, T. Przeorski, F. Hisker and S. Divinski: 'Titanium tracer diffusion in grain boundaries of α-Ti, α_2-Ti_3Al, and γ-TiAl and in α_2/γ interphase boundaries', *Intermetallics*, 2001, **9**, 431–442.
29. M. Volante, B. Fubini, E. Giamello and V. Bolis: 'Reactivity induced by grinding in silicon nitride', *J. Mater. Sci.*, 1989, **8**, 1076–78.
30. I. J. Lin and S. Nadiv: 'Review of the phase transformation and synthesis of inorganic solids obtained by mechanical treatment (mechanochemical reactions)', *Mater. Sci. Eng.*, 1979, **39**, 193–209.
31. P. Yu. Butyagin: 'Mechanochemical reactions of solids with gases', *React. Solids*, 1986, **1**, 345–359.
32. R.-M. Ren, Z.-G. Yang and L. Shaw: 'Synthesis of nanostructured silicon carbide through integrated mechanical and thermal activation process', *J. Am. Ceram. Soc.*, 2002, **85**, 819–827.
33. L. Shaw, Z.-G. Yang and R.-M. Ren: 'Mechanically enhanced reactivity of Si for the formation of Si_3N_4 composites', *J. Am. Ceram. Soc.*, 1998, **81**, 760–764.
34. C. Greshovich and J. H. Rosolowski: 'Sintering of covalent solids', *J. Am. Ceram. Soc.*, 1976, **59**, 336–343.
35. P. Comley: 'Multi-rate superplastic forming of fine grain Ti–6Al–4V titanium alloy', *J. Mater. Eng. Perform.*, 2007, **16**, 150–154.
36. X. Song, X. Liu and J. Zhang: 'Neck formation and self-adjusting mechanism of neck growth of conducting powders in spark plasma sintering', *J. Am. Ceram. Soc.*, 2006, **89**, 494–500.
37. R. Chaim, M. Levin, A. Shlayer and C. Estournès: 'Sintering and densification of nanocrystalline ceramic oxide powders: a review', *Adv. Appl. Ceram.*, 2008, **27**, 159–169.
38. R. Orrù, R. Licheri, A. M. Locci, A. Cincotti and G. Cao: 'Consolidation/synthesis of materials by electric current activated/assisted sintering', *Mater. Sci. Eng. R*, 2009, **R63**, 127–287.
39. Z. A. Munir, D. V. Quach and M. Ohyanagi: 'Electric current activation of sintering: a review of the pulsed electric current sintering process', *J. Am. Ceram. Soc.*, 2011, **94**, 1–19.
40. E. Eriksson, Z. Shen and M. Nygren: 'Fast densification and deformation of titanium powder', *Powder Metall.*, 2005, **48**, 231–236.
41. M. Zadra, F. Casari, L. Girardini and A. Molinari: 'Microstructure and mechanical properties of cp-titanium produced by spark plasma sintering', *Powder Metall.*, 2008, **51**, 59–65.
42. G. L. Carr, S. Perkowitz and D. B. Tanner: 'Far-infrared properties of inhomogeneous materials', in 'Infrared and millimeter waves', Chap. 6, 184; 1985, Orlando, FL, Academic Press.